Journal of
Marine Science and Engineering

MDPI

Article

Long-Term Trends of Sea Surface Wind in the Northern South China Sea under the Background of Climate Change

Bo Hong [1,2,*] and Jie Zhang [1,*]

1 School of Civil Engineering and Transportation, South China University of Technology, Guangzhou 510641, China
2 Southern Marine Science and Engineering Guangdong Laboratory (Zhuhai), Zhuhai 519000, China
* Correspondence: bohong@scut.edu.cn (B.H.); 201821009440@mail.scut.edu.cn (J.Z.)

Abstract: The long-term trends of sea surface wind are of great importance to our understanding of the effects of climate change on the marine environment. In the northern South China Sea (SCS), the long-term changes in coastal sea surface wind are not well-understood. Based on the latest reanalysis (ERA5) data from 1979 to 2019, our analysis showed a decreasing trend in the annual mean wind speed in the coastal area and an increasing trend in the open sea. There was a significant weakening trend in the easterly wind component in the coastal and continental shelf areas, whereas there was an increasing trend in the northerly wind component in the open sea. The Mann–Kendall mutation analysis suggested that there were significant changes in the wind speed and frequency of strong wind. Significant correlations were found between the variation of the wind field and El Niño–Southern Oscillation by wave coherence analysis. The strengthening of the wind stress curl was an important factor for the enhancement of coastal upwelling along the coast of the northern SCS. The wind field plays an important role in modulating the climatic change of significant wave height.

Keywords: long-term trend; sea surface wind; South China Sea; climate change; ERA5

Citation: Hong, B.; Zhang, J. Long-Term Trends of Sea Surface Wind in the Northern South China Sea under the Background of Climate Change. *J. Mar. Sci. Eng.* **2021**, *9*, 752. https://doi.org/10.3390/jmse9070752

Academic Editor: Kyung-Ae Park

Received: 15 May 2021
Accepted: 29 June 2021
Published: 7 July 2021

1. Introduction

Climate change has become a prominent focus for both marine and atmospheric research worldwide. Global warming has resulted in different degrees of temperature increase in the oceans and on land. Such a temperature change alters the monsoon system and thus causes changes in the sea surface wind, ocean currents, sea surface temperature (SST) and precipitation, among other factors, over different timescales [1–7]. The South China Sea (SCS) is a marginal sea of the western Pacific Ocean. It resides at the junction of the Eurasian, Pacific and Indo-Australian plates (Figure 1). The East Asian monsoon prevails over the SCS. The location of the SCS makes it highly sensitive to climatic changes in atmospheric–marine processes [7,8]. Investigating the long-term trends of sea surface wind in the SCS is important for understanding the effect of climate change on the local marine environment.

Many studies have focused on the change in the East Asian monsoon in response to climate change. Using the monsoon intensity index, Shi [9] investigated the trend of winter monsoon intensity in East Asia from 1950 to 1989 and found that the winter monsoon showed a decreasing trend while the temperature in mainland China showed a clear increasing trend. Analyses of the daily ground data from 194 stations and the National Centers for Environmental Prediction (NCEP)/National Center for Atmospheric Research (NCAR)'s reanalysis data indicated that the southwest monsoon intensity in China decreased rapidly from 1957 to 1978 and then increased from 1979 to 2000, whereas the southeast monsoon intensity decreased consistently from 1957 to 2000 [10]. After analyzing the observed data at meteorological stations, Jiang et al. [11] found that the temperature and pressure difference between the Asian continent and the Pacific Ocean decreased significantly owing to global warming. Therefore, the East Asian monsoon weakens in both winter and summer, which leads to the weakening of the average wind speed. The results also indicated decreasing trends, albeit different in different regions, in the annual mean wind speed, days of wind gusts and maximum wind speed in mainland China. Jiang et al. [12] used the global climate model to predict the future trends of wind in China and indicated that, compared with that in 1981–2000, the maximum wind speed will decrease in 2046–2065 and 2080–2099. After exploring the meteorological observation data from 1961 to 2012, Shi et al. [13] also demonstrated a weakening trend in wind speed in Guangdong Province (adjacent to the southern coast of China; Figure 2a). In addition, the analysis of 51 years of data (1961–2012) from the Guangzhou meteorological observation station showed a weakening trend in the local annual maximum wind speed [14]. Using NCEP/NCAR and ERA40 data from 1948 to 2007, Wang et al. [1] analyzed the winter monsoon wind speed at 850 hPa and found no significant changes in the long-term trend of the meridional wind component over the central SCS. However, both reanalysis datasets showed a significant increasing trend in the easterly wind component. The wind indices defined in the lower troposphere during the summer monsoon period showed a coherent decreasing trend from 1960 to 1998, thereby suggesting a weakening SCS summer monsoon [15–17].

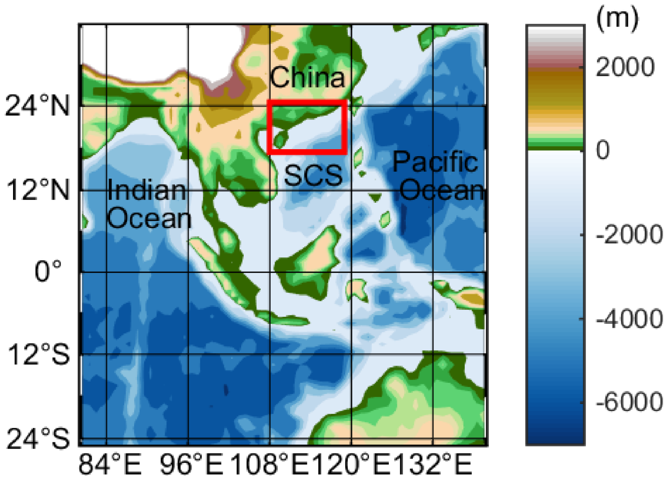

Figure 1. Bathymetry of the South China Sea (SCS). The northern SCS is denoted by the red rectangle.

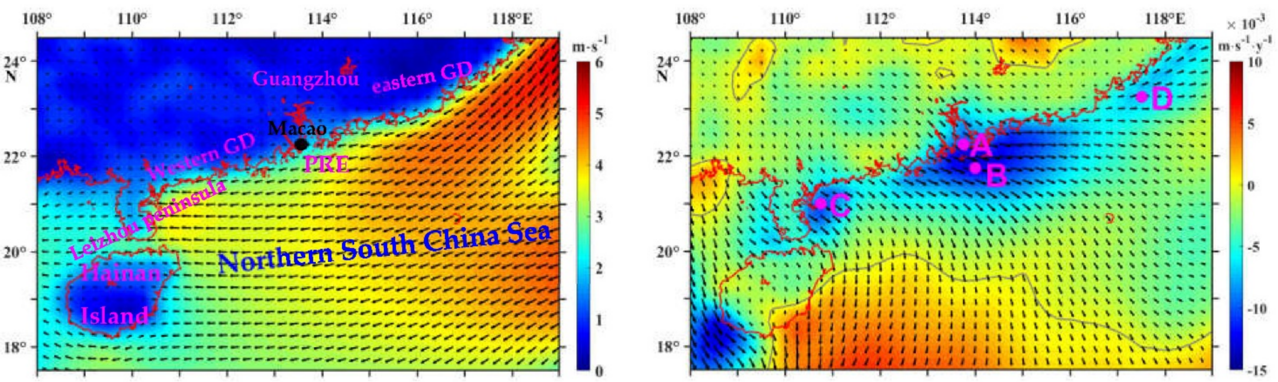

(a) (b)

Figure 2. Spatial distribution of the annual mean wind field and its trend in the northern South China Sea from 1979 to 2019. (**a**) Annual mean wind field (contours indicate the wind speed); (**b**) Trend of the annual mean wind speed (shaded colors; grey contours represent 0, and negative values represent a decreasing trend) and trend of the wind vectors, which were obtained by calculating the trend of the zonal wind component (u) and the meridional wind component (v), respectively (represented by vectors). PRE: Pearl River Estuary. GD: Guangdong Province. Four representative stations, namely A (22.25° N, 113.75° E), B (21.75° N, 114.00° E), C (21.00° N, 110.75° E) and D (23.00° N, 117.50° E) in (**b**) are used for later analyses.

From the perspective of global change, the sea surface wind showed significant spatial and temporal variations. Ward et al. [18] found no clear trend of sea surface wind speed in the second half of the 20th century but found a decreasing trend in the equatorial waters, South Atlantic tropical waters and North Pacific tropical waters. Gulev et al. [19,20] found a strong increasing trend in wind speed in the middle latitudes of the North Atlantic from 1964 to 1993 but found no significant trend in the Northeast Atlantic. After analyzing the buoy data provided by the Meteorological Service of Canada and the National Data Buoy Center of the United States, Gower [21] revealed an increasing trend in the sea surface wind speed in the high latitude area of the North Pacific from 1977 to 1999. Using satellite assimilation data from 1991 to 2008, Young et al. [22] studied the trend of global sea surface wind speed and found an increasing trend in many areas worldwide, with the increasing trend in extreme wind speed being more significant. Islek et al. [6] used 40 years (1979–2019) of ERA-Interim and CFSR data to analyze the temporal and spatial variation characteristics of the wind field in the Black Sea. Their results showed that the wind fields in the western and northern Black Sea were stable and continuous, whereas those in the eastern Black Sea were complex and volatile owing to climate change.

Most studies have focused on the temporal and spatial variations of sea surface wind and the dynamic mechanisms of the SCS monsoon outbreak. However, the long-term trends of wind speed and direction in the northern SCS, especially in the Pearl River Estuary (PRE) and the coastal upwelling area, are unclear. Some physical processes, such as coastal upwelling, river plume transport and estuarine circulation, are controlled by local wind forcing. The long-term trends of sea surface wind in the local hotspot areas should be thoroughly investigated. Changes in the wind field due to climate change could significantly affect the estuarine ecosystem. Wilson et al. [23] indicated that climatic processes, namely the long-term changes in both the direction and directional constancy of summertime winds, control the ventilation of bottom waters and thus the seasonal development of hypoxia in the western Long Island Sound. Scully [24] also indicated that the decadal-scale variability of climate forcing caused the change in wind direction over the Chesapeake Bay, which was responsible for the increased hypoxic volume from the early 1980s to the present. Assessing the trends of sea surface wind is important for understanding the response of the marine environment to climate change.

In this study, we used the latest European Centre for Medium-Range Weather Forecasts (ECMWF) fifth-generation reanalysis (ERA5) data to analyze the long-term trends of the wind field in the northern SCS over the past 41 years (1979–2019). The results of this study will help to reveal the long-term trends of sea surface wind and their effect on the local marine environment in the northern SCS against the background of climate change.

The remainder of this paper is organized as follows: Section 2 introduces the data and methods. Section 3 presents the results and discussion. Section 4 summarizes the conclusions.

2. Study Area

The northern SCS has a coastline in the northeast–southwest direction (Figure 1). It is connected to the Pacific Ocean and the East China Sea through the Luzon Strait and the Taiwan Strait, respectively. The wind field in the northern SCS has strong regional and seasonal characteristics. Wind forcing is an important factor affecting the marine environment. As the most important estuary in the northern SCS, the PRE discharges large amounts of fresh water, nutrients, sediment and terrestrial pollutants into the northern SCS [25–28]. The numerical model results obtained by Pan et al. [29] indicated that the wind direction affects the generation of plumes in the PRE. Therefore, the trend of the wind field in the PRE was the main focus of this study. In addition, there is significant upwelling along the east coast of Hainan Island and eastern Guangdong [30–34]. Coastal upwelling can transport nutrients to the sea surface and promote the growth of phytoplankton, zooplankton and other organisms, thereby forming a better fishing ground. Studies have indicated that the summer southwesterly monsoon is the main factor affecting the upwelling intensity along the northern coast of the SCS [30,31]. Analyzing the wind trends in the coastal upwelling area was another focus of this study.

3. Data and Methodology

3.1. Data

The trends of sea surface wind in the northern SCS were investigated using the latest ERA5 hourly and monthly wind data at 10 m above the sea surface. The SST and significant wave height data from ERA5 were also used to evaluate the responses of the marine environment to the changes in the wind regime. ERA5 is the global reanalysis product produced by ECMWF. The ECMWF reanalysis began in 1979, followed by the production of ERA15 in the mid-1990s, ERA40 from 2001 to 2003, and ERA-Interim from 2006 to 2019 [35]. ERA5 is based on a hybrid incremental 4D-Var system [36], which uses observations from over 200 satellite instruments or types of conventional data. The spatial and temporal resolutions of ERA5 are $0.25^\circ \times 0.25^\circ$ and 1 h, respectively. ERA5 has higher spatial and temporal resolutions than the previous four generations of datasets.

3.2. Methodology

3.2.1. Mann–Kendall Test

The Mann–Kendall (M–K) test was used to detect the change point of the wind field. The M–K test is a climatic change-point analysis method that is widely used in meteorological and hydrological time series [37–40]. It is a nonparametric test that requires the data to be independent and to tolerate outliers. UF and UB are two M–K statistics used to indicate the trend and the change point in the data. Given a time series $x_1, x_2, \ldots, x_n$,

$$d_k = \sum_{i=1}^{k} m_i, \ (2 \leq k \leq n) \tag{1}$$

where:

$$m_i = \begin{cases} +1, x_i > x_j \\ 0, x_i \leq x_j \end{cases}, j = 1, 2, \ldots, i \tag{2}$$

UF_k is calculated as follows:

$$UF_k = \frac{d_k - E(d_k)}{\sqrt{\mathrm{Var}(d_k)}} \ (k = 2, 3, \ldots, n), \tag{3}$$

when $k = 1$ and $UF_1 = 0$. UB_k is calculated with the reverse sequence. The change point of the time series is defined as the point where the curves of UF and UB intersect within the confidence interval. UF and UB obey the normal distribution. With the significance level $\alpha = 0.05$, the critical value of UF and UB is ± 1.96 [41]. A negative UF value indicates a decreasing trend, whereas a positive UF value indicates an increasing trend. The trend changes significantly if UF and UB exceed the critical value.

3.2.2. Cross-Wavelet Transform

This study investigated the correlation between the wind field and the El Niño–Southern Oscillation (ENSO). The Oceanic Niño Index (ONI) provided by the National Oceanic and Atmospheric Administration is used to indicate the intensity of ENSO. Two major steps of our analysis were (1) empirical orthogonal function (EOF) analysis and (2) cross-wavelet transform (XWT) analysis. First, the major spatiotemporal patterns of the wind field were identified using the EOF method, which were used to extract significant space–time signals from the wind data. XWT was then used on the EOF time coefficients and ONI to determine the correlation between the wind field and ENSO.

XWT analysis is a signal analysis method that combines cross-spectrum analysis with wavelet transform [42]. It can effectively reflect the time–frequency correlations between two time series and reveal their resonance period and phase relationship at multiple timescales [43]. Given two time series, X_i and Y_i, XWT is calculated as follows:

$$W_i^{xy}(s) = W_i^{x}(s) W_i^{y*}(s) \quad (4)$$

where $W_i^{y*}(s)$ is the complex conjugate of $W_i^{y}(s)$ and s is the wavelet scale. The cross-wavelet power is defined as $\left|W_i^{XY}\right|$, which represents the power resonance information of X_n and Y_n in the time–frequency domain. A higher power value represents a stronger correlation between the high energy region of X_n and Y_n.

Wavelet coherence (WTC) is based on the continuous wavelet transform and XWT of two time series to reflect the time–frequency correlation degree. It is calculated as follows:

$$R_i^2(s) = \frac{\left|S\left(s^{-1}W_i^{XY}(s)\right)\right|^2}{S\left(s^{-1}\left|W_i^{X}(s)\right|^2\right)' S\left(s^{-1}\left|W_i^{Y}(s)\right|^2\right)}, \quad (5)$$

where S is the smooth operator. In this study, the Morlet wavelet was selected as the wavelet function. Morlet wavelets have non-orthogonality, provide a good balance between time and frequency localization and contain more vibration information [44].

4. Results and Discussion

4.1. Spatial Variation of the Wind Field in the Northern SCS

The annual mean wind fields averaged from 1979 to 2019 are shown in Figure 2a. Owing to the morphologic effect of the Taiwan Strait and the Luzon Strait, the wind speed in the northeastern SCS was significantly stronger than that in other areas [45]. The wind speed decreased gradually from the northeast to the southwest. The northeasterly wind occupied the eastern portion of the northern SCS, whereas the easterly wind appeared in the western portion, especially in the offshore area of western Guangdong Province and eastern Hainan Island.

The trend of the annual mean wind speed over the past 41 years in the northern SCS was calculated using least-squares regression. The trend of the annual mean wind speed (Figure 2b) showed significant spatial variations. A clear decreasing trend was observed in the coastal area. In the PRE and its adjacent sea, the maximum rate of decrease was -0.015 m·s^{-1}·y^{-1}. A slightly weaker rate of decrease of approximately 0.01 m·s^{-1}·y^{-1} appeared over the coastal waters of the Leizhou Peninsula and eastern Guangdong. The rate of decrease southwest of Hainan Island was also -0.015 m·s^{-1}·y^{-1}. The decreasing trend in wind speed gradually weakened from the coastal area to the open sea. An increasing trend gradually appeared around 18° N–19° N, and the increasing trend offshore of southeast Hainan Island was stronger than that in other areas.

To assess the long-term changes in the annual mean wind direction, the trends of wind vectors were obtained by calculating the trends of the zonal wind component (u) and the meridional wind component (v). The resulting trend vectors represent the change in wind direction and also help to illustrate the contribution of each wind component to the long-term trends of wind speed. As shown in Figure 2a, the annual mean wind was generally northeasterly or easterly ($u > 0$). Thus, the trends of wind vectors shown in Figure 2b indicate that the zonal wind component decreased, which meant that the easterly wind component weakened over the past 41 years. The weakening of the easterly wind was more notable in the coastal and continental shelf areas than in the open sea. However, the meridional wind increased, which meant that the northerly wind component strengthened. The strengthening of northerly wind was more significant in the open sea than in the coastal area. Thus, the decreasing trend in wind speed in the coastal sea was due to the weakening of easterly wind, whereas the increasing trend in wind in the open sea was due to the strengthening of the northerly wind.

The monthly mean wind fields are shown in Figure 3a. Dominated by the East Asian monsoon, the sea surface wind over the northern SCS showed clear seasonal variations.

A strong northeasterly wind appeared in the winter months (December, January and February) and a strong southerly/southwesterly wind appeared in the summer months (June, July and August). The spring and autumn months are the monsoon transition period. The trends of the monthly mean wind fields showed remarkable seasonal variations (Figure 3b). The wind speed over the continental shelf area showed an increasing trend in December and January and a decreasing trend in February. The trends in the spring (March to May) and summer (June to August) months showed complex spatiotemporal variations. In March, the wind speed showed an increasing trend in almost the entire northern SCS. The highest growth rate of 0.035 $m \cdot s^{-1} \cdot y^{-1}$ appeared in the southeast corner. The wind vectors showed a remarkable increasing trend in the northerly wind component, indicating the strengthening of the northerly wind. In April and May, the wind speed along the east coast of Guangdong showed a significant decreasing trend, the maximum rate of which reached -0.035 $m \cdot s^{-1} \cdot y^{-1}$. In June, the wind speed showed an increasing trend in the entire northern SCS. According to the wind vectors, both the meridional and zonal wind components showed increasing wind, indicating the strengthening of the southwesterly wind in June. In July and August, the wind speed in the continental shelf showed a decreasing trend. The decreasing trend in July was more significant (with a rate of -0.025 $m \cdot s^{-1} \cdot y^{-1}$) in the coastal upwelling area of eastern Guangdong and eastern Hainan Island. Such long-term trends could cause changes in the coastal upwelling process, which in turn could affect fishing in the northern SCS. The trends of the wind vectors indicated a decrease in the meridional wind, suggesting the weakening of the southerly wind in July and August. From September to November, the wind speed showed a decreasing trend over a large domain. The weakening of the easterly wind contributed to the decrease in wind speed in September and October, and the weakening of the northerly wind contributed to the decrease in wind speed in November.

4.2. Wind Field Trends in Typical Areas

According to the spatial distribution of the wind speed trend shown in Figure 2b, the decreasing trends in the PRE and the adjacent sea and coastal waters of the Leizhou Peninsula and eastern Guangdong were more significant than those in other areas. These hotspots were selected as representative areas to conduct further analyses. Four representative stations, namely A (22.25° N, 113.75° E), B (21.75° N, 114.00° E), C (21.00° N, 110.75° E) and D (23.00° N, 117.50° E), were chosen to analyze the long-term trends of the wind field.

To verify the reliability of our analysis, data recorded at Macau Airport (22.22°N, 113.50°E) during 1997–2015 were compared with ERA5 data at station A (located in the lower PRE, close to the Macao Airport). The monthly mean results were plotted in Figure 4. It can be seen that both the wind direction and speed are in good agreement between ERA5 data and airport observations. The annual mean wind speed and its trend from these two data sources also showed good consistency in both magnitude and trend (as shown in Figure 5a, subplot for station A). Therefore, the ERA5 dataset used in this study is robust in the coastal area. The annual mean wind speed at each station is shown in Figure 5a. The annual mean wind speed at each station showed a decreasing trend accompanied by significant interannual oscillation. The rates of decrease at stations A, B, C and D were -0.0106, -0.0130, -0.0102 and -0.0068 $m \cdot s^{-1} \cdot y^{-1}$, respectively. The PRE and its adjacent water had the greatest rate of decrease in the annual mean wind field. Wilson et al. (2008) indicated that the weakening of the wind field will weaken the mixing in the estuary, thereby enhancing water stratification. Such a condition prevents the transport of dissolved oxygen to the bottom of the estuary, thereby making the estuary more prone to hypoxic events. Hypoxia has frequently been reported during the summer in the PRE [26,46]. Our analyses also indicated a notable decreasing trend in wind speed in July in the PRE and adjacent waters (Figure 3b). The weakening wind in July is assumed to contribute to hypoxia in the PRE. Further research is needed to reveal the related dynamic mechanisms.

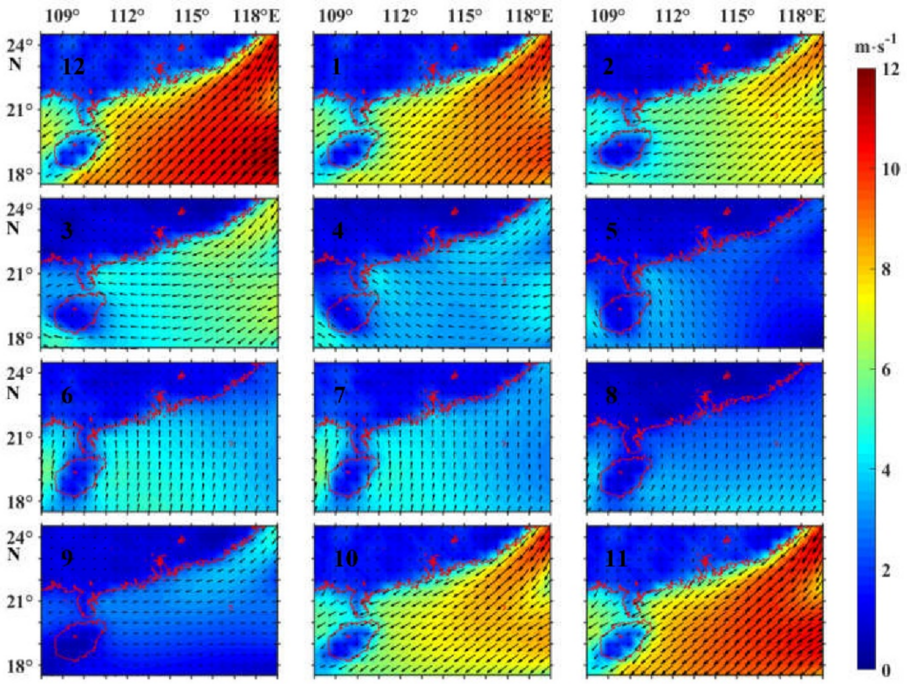

(a)

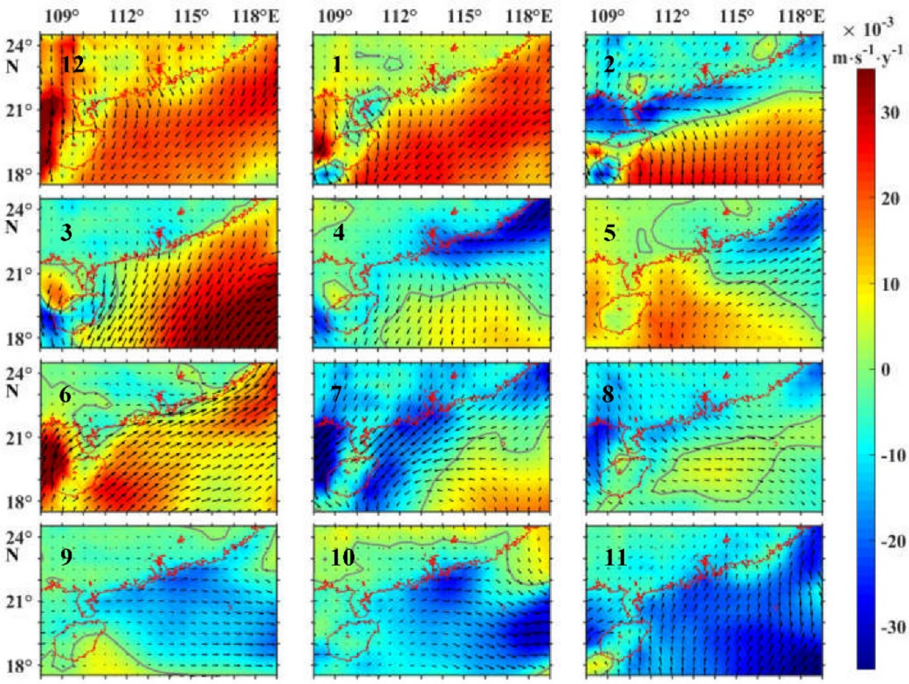

(b)

Figure 3. Spatial distribution of the monthly mean wind field (**a**) and its trend (**b**) in the northern South China Sea from 1979 to 2019.

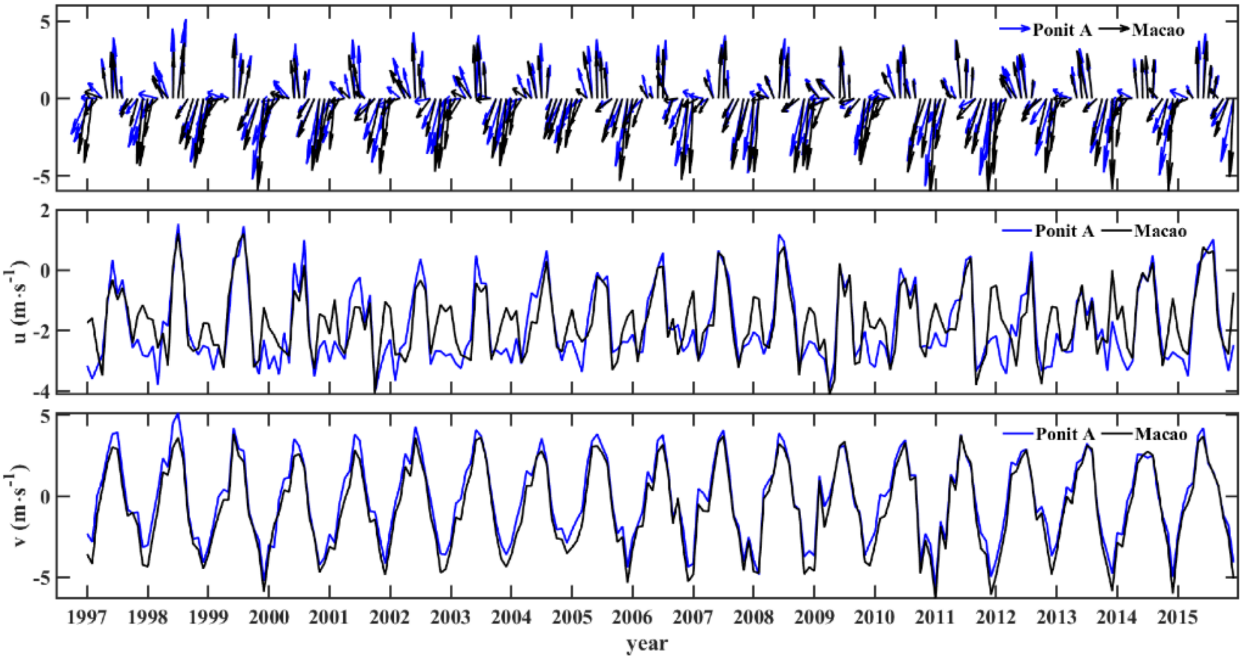

Figure 4. Comparisons of monthly mean wind vectors (**upper**), u-component (**middle**) and v-component (**lower**) of wind data from 1997 to 2015 obtained from ERA5 data at station A (blue) and observation data at Macao Airport (black). The location of station A is in the lower PRE and close to Macao Airport.

The quartile values (75%) of the daily mean wind speeds at stations A, B, C and D over 41 years were used as the strong wind standard at each station (Table 1). The strong wind days at each station were calculated as the days in each year with a daily mean wind speed greater than the standard value. The results are shown in Figure 5b. The strong wind days also showed decreasing trends at stations A, B and C. There was no significant trend at station D. The rates of decrease in strong wind days are listed in Table 1. The highest rate of decrease was at station A, which is located in the PRE. Strong winds play an important role in modulating the synoptic events in coastal hydrodynamic processes. The decrease in strong wind days in the estuary may significantly affect vertical mixing, lateral circulation, nutrient retention and sediment transport. Changes in the wind field must be taken into account when examining the long-term changes in coastal circulation and related environmental processes.

Table 1. Strong wind standard and the rate of change in strong wind days at stations A, B, C and D.

	A	B	C	D
Strong Wind Standard ($m{\cdot}s^{-1}$)	5.96	8.12	6.89	9.91
Rate of change in Strong Wind days ($d{\cdot}10\ y^{-1}$)	−9.73	−5.86	−7.40	−0.16

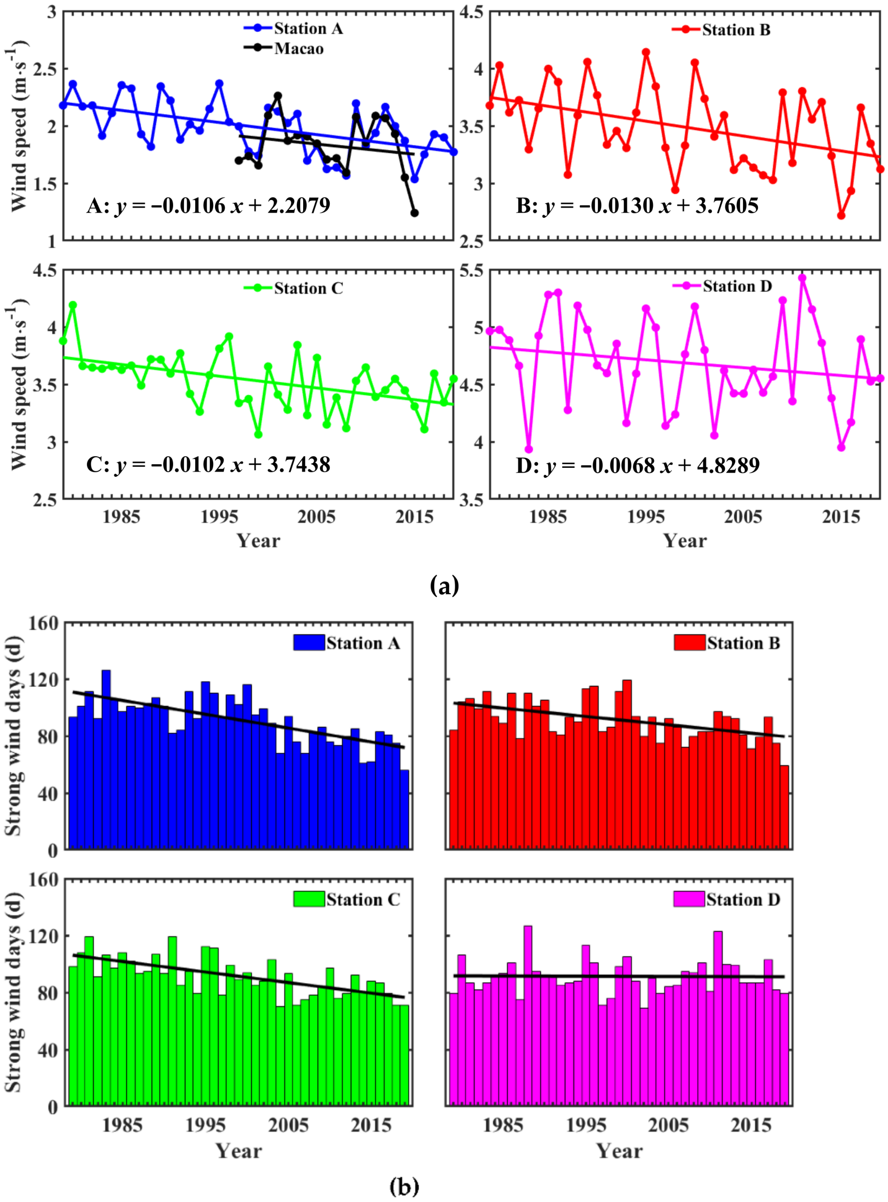

Figure 5. Trends of annual mean wind speed (**a**) and strong wind days (**b**) at station A, B, C and D, respectively, from 1979 to 2019. The annual mean wind speed and corresponding trend obtained from ERA5 data at station A were compared with the data obtained from the adjacent Macau Airport (from 1997 to 2015).

4.3. M–K Test of the Wind Fields in Representative Areas

M–K mutation analyses were conducted using the monthly mean wind speed at stations A, B, C and D. The algorithms for UF and UB were provided in Section 3, and the results were shown in Figure 6. At station A, the UF curve fluctuated from 1979 to 2002 and, since 2003, UF has been less than 0, indicating that the wind speed continuously decreased. UF passed the significance test after 2010, indicating that the decreasing trend was more significant after 2010. The UF and UB curves intersect around 2004, indicating that the wind speed change occurred around this time. The annual mean wind speed was 2.07 $m \cdot s^{-1}$ before the change point. After the change point, the wind speed decreased by 13% to 1.81 $m \cdot s^{-1}$. At station B, UF < 0 after 2004, indicating a decrease in wind speed. Similar to that at station A, the change point at station B also occurred around 2004. At station C, the wind speed decreased continuously after 1986 (UF < 0), and the change point occurred around 1994. There was no clear change point of wind speed at station D.

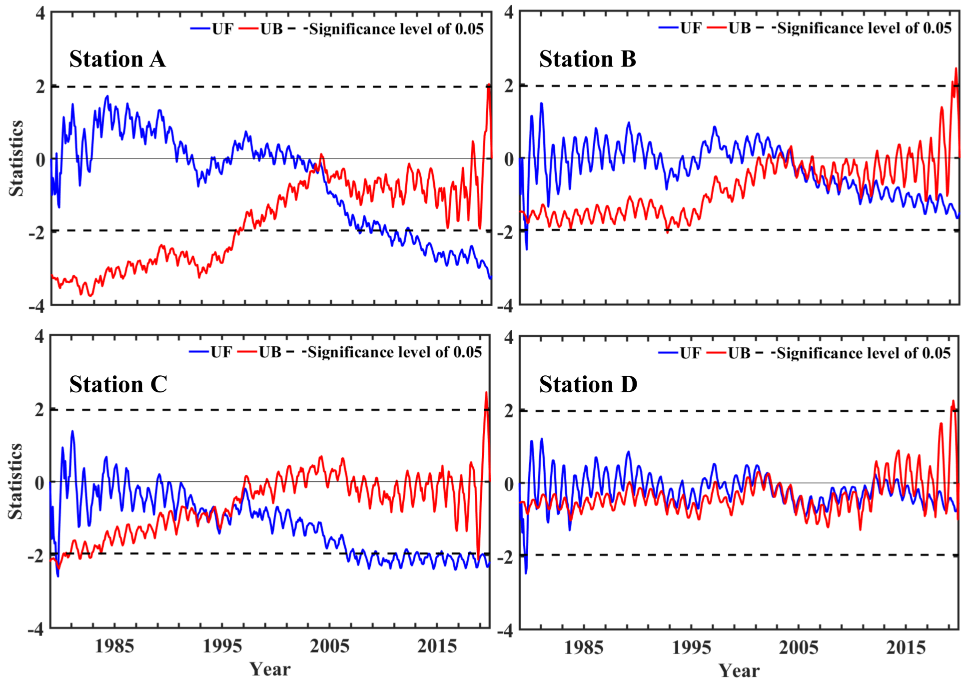

Figure 6. Mann–Kendall mutation analysis of monthly mean wind speed at station A, B, C and D, respectively, from 1979 to 2019. The UF and UB curves are shown in blue and red, respectively.

Further analyses of the wind field change before and after the change point were conducted using a wind rose diagram. The results for stations A, B and C are shown in Figure 7. The dominant wind directions at each station showed minor changes before and after the change point. Decreased easterly wind and increased northeasterly wind were discerned. However, the comparison of the frequency of strong winds (wind speed > 8 m·s^{-1}) before and after the change point indicated that the frequency of strong winds after the change point was lower than that before the change point. The strong wind frequency at stations A, B and C decreased by 1.25%, 4.10% and 2.86%, respectively. These results indicate that climate change has a significant effect on the wind speed and frequency of strong wind in the northern coastal area of the SCS but not on the wind direction.

4.4. Correlation between the Interannual Variation of the Wind Field and ENSO

The general 3–6 year periodicity of the SCS monsoon tends to match that of ENSO [1]. ENSO has a significant effect on the Pacific subtropical high and the Southeast Asian monsoon circulation. The EOF analysis decomposes the spatiotemporal variations of the geophysical field into a combination of orthogonal spatial patterns with corresponding principal components (PCs) in a linear fashion [47]. It serves as a powerful tool for identifying major modes of climate variability such as ENSO [48]. Figure 8 shows the EOF analysis of the normalized monthly mean sea surface wind speed in the northern SCS from 1979 to 2019. The leading mode accounted for 65.8% of the total variance, representing the spatial pattern corresponding to the distribution of the mean wind speed, which had a clear land–sea difference. The second and third modes accounted for 12.31% and 8.77% of the total variance, respectively. The spatial pattern of the second eigenvector reflects the phase difference between the coastal sea and open sea, whereas the spatial pattern of the third eigenvector reflects the phase difference between the northeastern and southwestern portions of the northern SCS. The wind speed in the eastern Guangdong coastal sea and the eastern Hainan coastal sea showed the opposite phase pattern.

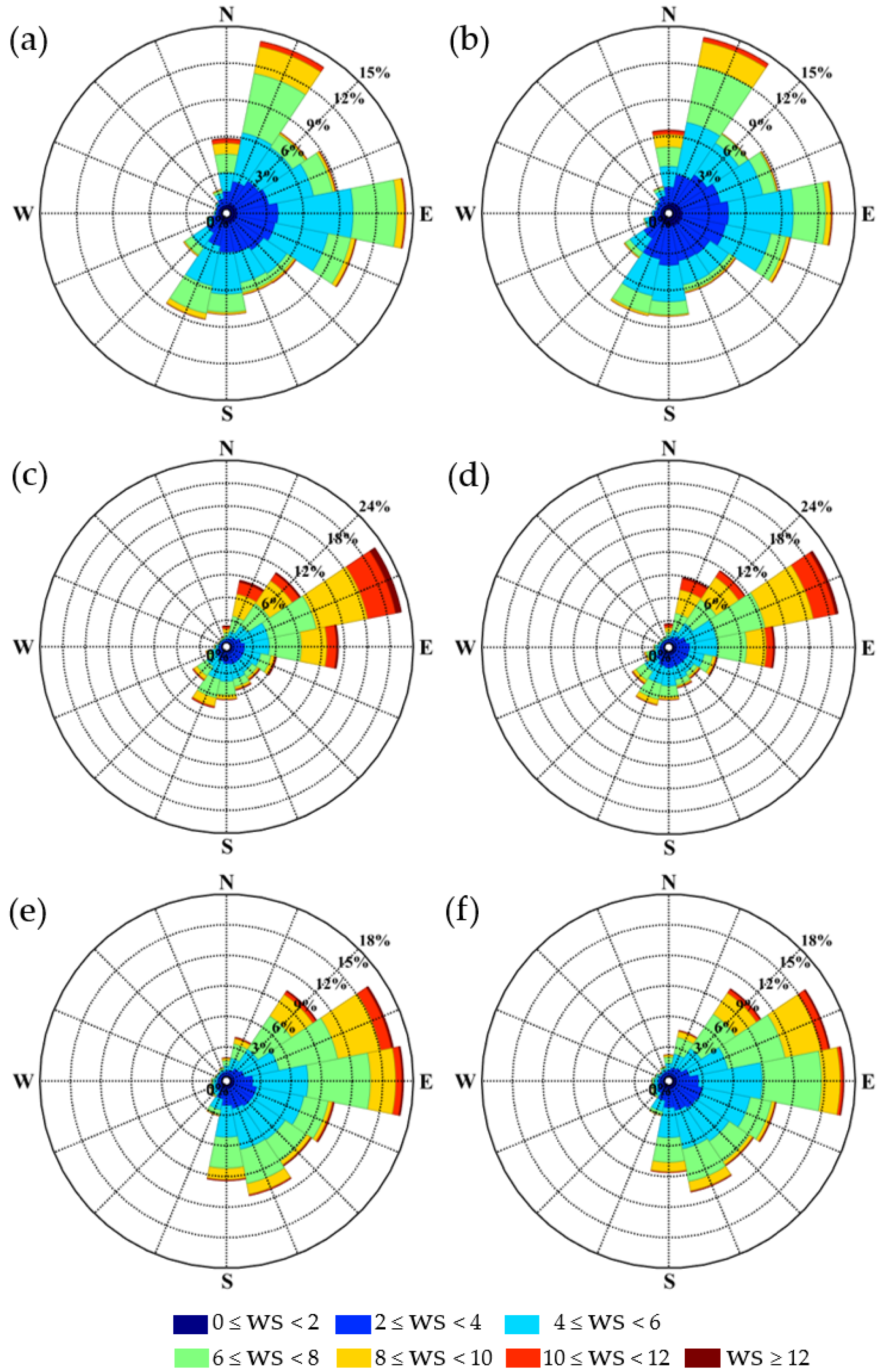

Figure 7. Wind rose before (left column) and after (right column) the change point of wind at station A (**a**,**b**), station B (**c**,**d**) and station C (**e**,**f**). WS represents wind speed.

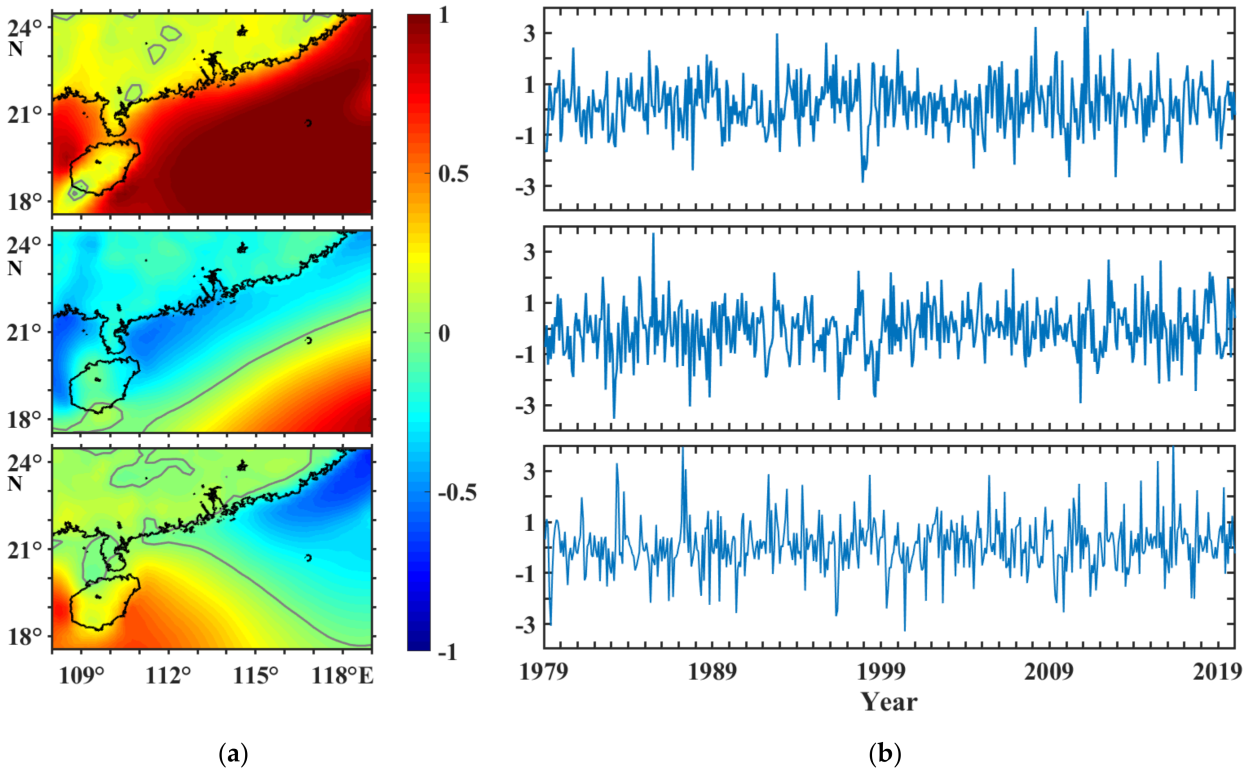

Figure 8. Spatial distribution of the eigenvectors and corresponding time coefficients of the first (**upper**), second (**middle**) and third (**bottom**) modes of the wind field empirical orthogonal function decomposition in the northern South China Sea. (**a**) Spatial distribution of eigenvectors; grey contours represent 0. (**b**) Time coefficients.

The wind speed in the northern SCS exhibits large year-to-year variations, which can be clearly seen from the PCs (Figure 8). Previous studies indicated that ENSO was the dominant factor that controls the interannual variation of the SCS monsoon [1,49]. In order to identify the dominant frequency of northern SCS wind speed variations that are related to the ENSO, the corresponding PCs of each mode were used to conduct the correlation analysis with ONI using XWT and WTC in the time and frequency domains. Generally, the results of XWT revealed the frequency of wind speed change in the northern SCS that could be accounted for by ENSO, whereas the results of WTC identified the period during which the wind speed variations were significantly correlated with ENSO. For the first mode (PC1), the result of XWT (Figure 9a) indicated that the wind speed and ENSO had significant common power in the frequency of the 2–6 year band from 1984 to 2002 and in the 1–4 year band after 2002. The PC1 and ENSO showed significant negative correlation in the period of 3–6 years during the 41 years (Figure 9b). This is consistent with the results of Wang et al. [1]. The XWT of the second mode (PC2) and ONI showed significant common power in the frequency of the 2–6 year band from 1981 to 1993 with the wind field change ahead of ENSO for approximately 3/8 periods. After 1993, the wind field change was ahead of ENSO for approximately 1/8 periods (Figure 9c). The corresponding WTC analysis (Figure 9d) showed multiple periods with high coherence, such as 1–2 years during 1991–1999, 3–6 years during 1983–1994 and 6–7 years after 2000. The second mode represented the phase difference of wind speed distribution between the coastal sea and the open sea. The result in Figure 9d indicated that the variations of the second mode wind speed did not have a consistent correlation with ENSO before 2000. After 2000, a good correlation can be found in the period of 6–7 years. For the third mode (PC3), the result of XWT (Figure 9e) indicated significant power in the frequency of the 3–6 year band from 1983 to 2004 and in the 1–2 year band discontinuously with various phase differences in different periods. The corresponding WTC result (Figure 9f) showed strong coherence in the 4–6 year band and a positive correlation of PC3 and ENSO can be discerned. The third mode represents the phase difference of wind speed distribution between the northeastern and southwestern portions of the northern SCS. The results revealed that the interannual variations of the third mode had a positive correlation with ENSO in a period of 4–6 years.

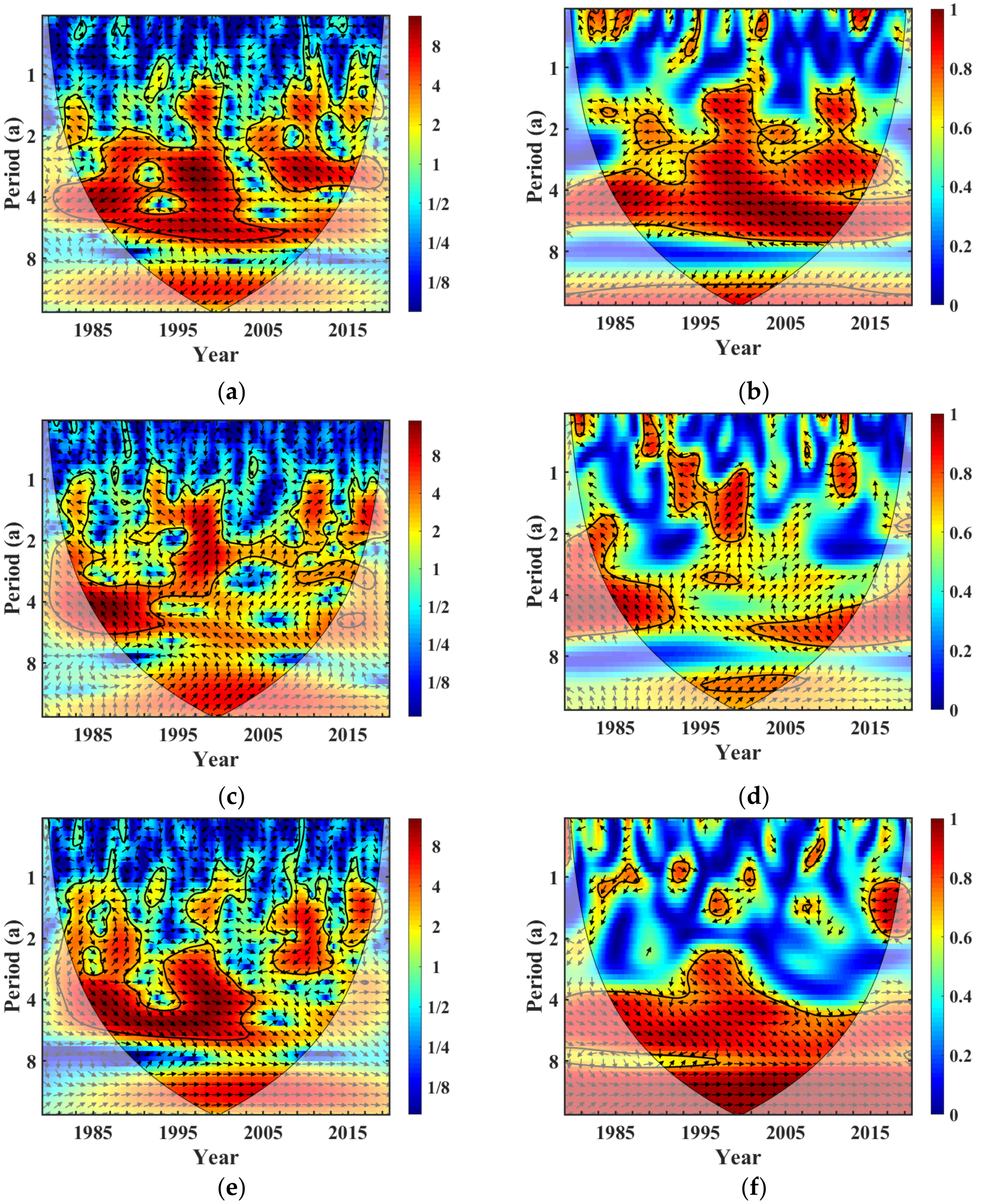

Figure 9. Correlations between the Oceanic Niño Index (ONI) and wind field principal components over the northern South China Sea. (**a**,**b**) First mode; (**c**,**d**) second mode; and (**e**,**f**) third mode. Left column: cross-wavelet transform. Right column: wavelet coherence.

4.5. Long-Term Trends of Wind Stress Curl and Effects on Coastal Upwelling

Jing et al. [30] indicated that both the alongshore wind stress and the wind stress curl play significant roles in coastal upwelling in the eastern Hainan and eastern Guangdong coastal seas. Coastal upwelling is a ubiquitous, monsoon-driven physical process that occurs along the continental shelf of the northwestern SCS [31]. It is important to examine the long-term trends of wind stress curl in the northern SCS to assess its effect on coastal upwelling. The spatial distribution of the summer wind stress curl, averaged from 1979 to 2019, is shown in Figure 10a. The wind stress curl was positive in both the eastern Hainan and eastern Guangdong coastal seas, in which typical coastal upwelling exists. The maximum wind stress curl was 3×10^{-7} N$\cdot \times$ m^{-3} in eastern Hainan. The high wind stress curl is expected to induce strong Ekman pumping in this area, which is conducive to upwelling. The trend of summer wind stress curl, shown in Figure 10b, indicated a strong increasing trend (with a rate of approximately 1×10^{-9} N$\cdot \times$ m$^{-3}\cdot$y^{-1}) in the coastal area, especially in the eastern Hainan and eastern Guangdong coastal seas.

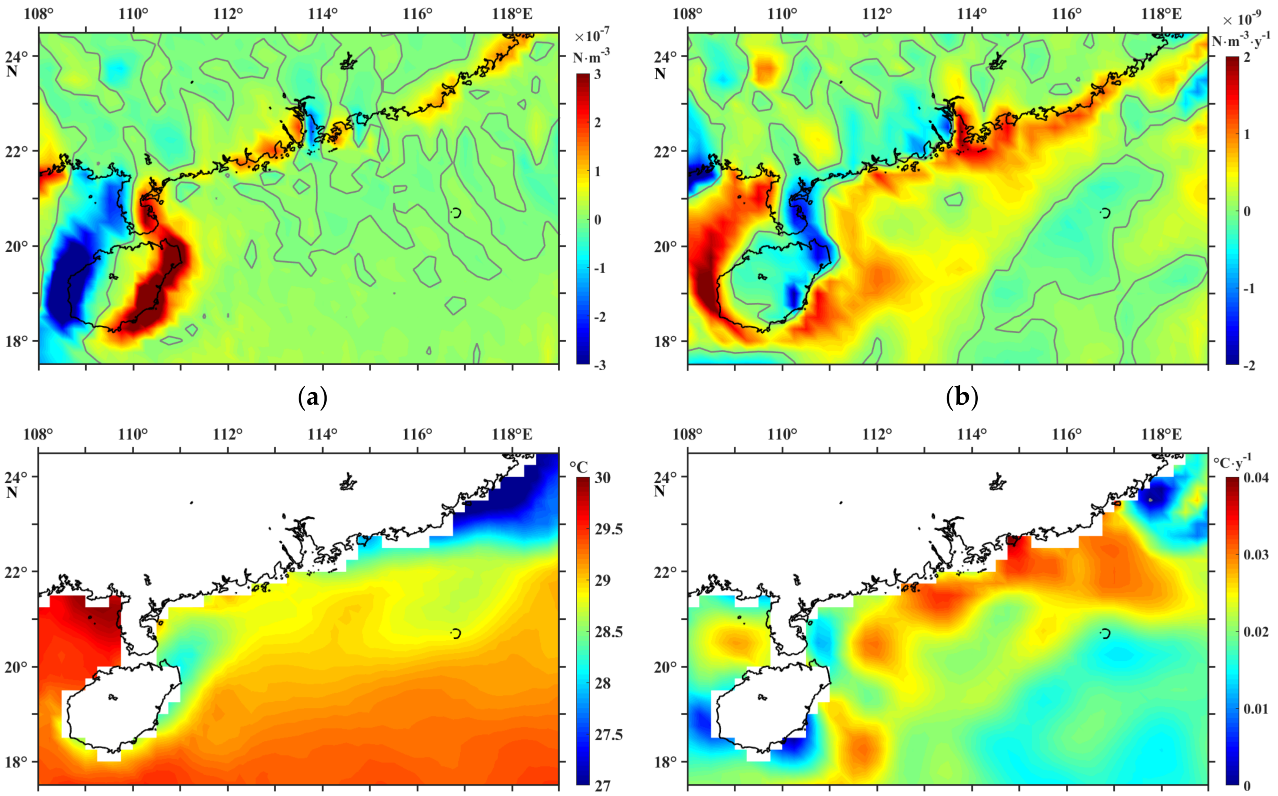

(a) (b) (c) (d)

Figure 10. (**a**) Spatial distribution of the summer mean wind stress curl averaged from 1979 to 2019. (**b**) Trend of the summer mean wind stress curl. (**c**) Spatial distribution of the summer mean sea surface temperature (SST) averaged from 1979 to 2019. (**d**) Trend of the summer mean SST. The grey contours represent 0.

Water that rises to the surface as a consequence of upwelling is usually colder than the surface water. The summer mean SST averaged from 1979 to 2019 is shown in Figure 10c. Two typical coastal upwelling regions can be discerned. One is the eastern Hainan coastal upwelling area, where the SST was approximately 28.0 °C—approximately 1.5 °C colder than the surrounding water. The other one is the eastern Guangdong coastal upwelling area, where the SST was approximately 27 °C—approximately 1 °C colder than the surrounding water. Figure 10d presents the long-term trends of SST. The summer SST in the northern SCS showed a warming trend against the background of global warming. Spatial variations can be found in the SST trend. The warming trend was stronger in the Guangdong coastal sea. The maximum warming rate was 0.35 °C$\cdot$y^{-1}. The rates of increase in SST in the two typical upwelling regions were lower than those in other areas, which indicated that the SST difference between the upwelling area and the ambient area increased. The coastal upwelling strengthened from 1979 to 2019.

Coastal upwelling is an important driving force of the spatial distribution of zooplankton abundance [50,51]. It occurs when alongshore wind stress produces offshore Ekman transport [$= \tau_{alongshore}/(\rho f)$, where $\tau_{alongshore}$ is the alongshore component of surface wind stress, ρ is the seawater density and f is the Coriolis parameter] or when the wind stress curl produces upward motion at the bottom of the Ekman layer. Figure 10 indicated that the strengthening of coastal upwelling in the two typical coastal upwelling regions of the northern SCS was in good agreement with the increasing trend of the positive wind stress curl at the same sites. Although the increasing trend of wind stress curl can also be found around the PRE and its adjacent coastal sea, the corresponding wind stress curl is not positive and there are no obvious upwelling processes. Wind stress, which is proportional to the Ekman transport [52], showed a decreasing trend in July and August along the coast of the northern SCS (Figure 3b). Our results indicated that the strengthening of the positive wind stress curl was responsible for the strengthening of coastal upwelling at eastern Hainan Island. Further numerical model research is needed to evaluate the relative importance of long-term changes in alongshore wind stress and wind stress curl to the long-term changes in coastal upwelling in eastern Guangdong.

4.6. Effect of the Trend of Wind Stress on Significant Wave Height

The spatial distribution of the annual mean significant wave height (averaged from 1979 to 2019) in the northern SCS is shown in Figure 11a. The spatial distribution of the significant wave height was closely related to the spatial variation of the seabed topography. The wave height in the coastal shallow waters was lower than that in the offshore deep waters owing to energy dissipation in the shallow area. The spatial distribution of the long-term trends of annual mean wave height (Figure 11b) showed an increasing trend in the open sea, which gradually weakened towards the coast of the northern SCS. A decreasing trend was seen in the coastal area, consistent with the decreasing trend in wind speed shown in Figure 2b.

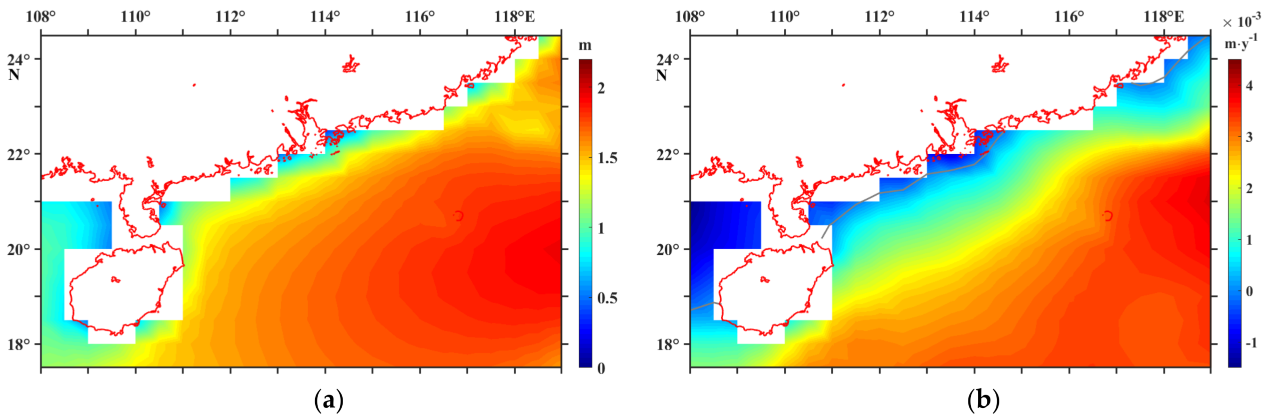

Figure 11. (**a**) Spatial distribution of the annual mean significant wave height in the northern South China Sea averaged from 1979 to 2019. (**b**) Trend of the annual mean significant wave height. Grey contours represent 0.

Waves in the SCS are influenced by the East Asian monsoon and thus show a significant seasonal difference [53,54]. The spatial distributions of seasonal mean wind speed (Figure 12a) and significant wave height (Figure 12b) showed similar seasonal variations. The high wave height in autumn and winter was consistent with the high wind speed during these seasons. The long-term trends of the seasonal mean wind speed (Figure 12c) showed a similar pattern to that of the seasonal mean significant wave height (Figure 12d). In spring and summer, the wave height showed a decreasing trend in the coastal area and an increasing trend in the offshore area. The decreasing trend was present in almost the entire northern SCS in autumn. In winter, a significant increasing trend was observed throughout the domain. Similar spatial patterns were found for the long-term trend of seasonal mean wind speed, which plays an important role in the change in wave height, which in turn may influence ocean engineering in the long term. The long-term reduction in wave height could also be related to the oceanic conditions [55] (Shimura et al., 2016) and extreme weather [4]. Studies in other oceans/seas have also indicated that the long-term trend of wave height showed clear spatial [56] (Aydogan and Ayat, 2018) and seasonal [57] (Zheng and Li, 2015) variations. Wind and wave energy are important for renewable energy, ocean engineering and coastal protection. Long-term changes in wind and waves also affect the coastal topography and the shape of beaches. Their variability and responses to climate change require further exploration.

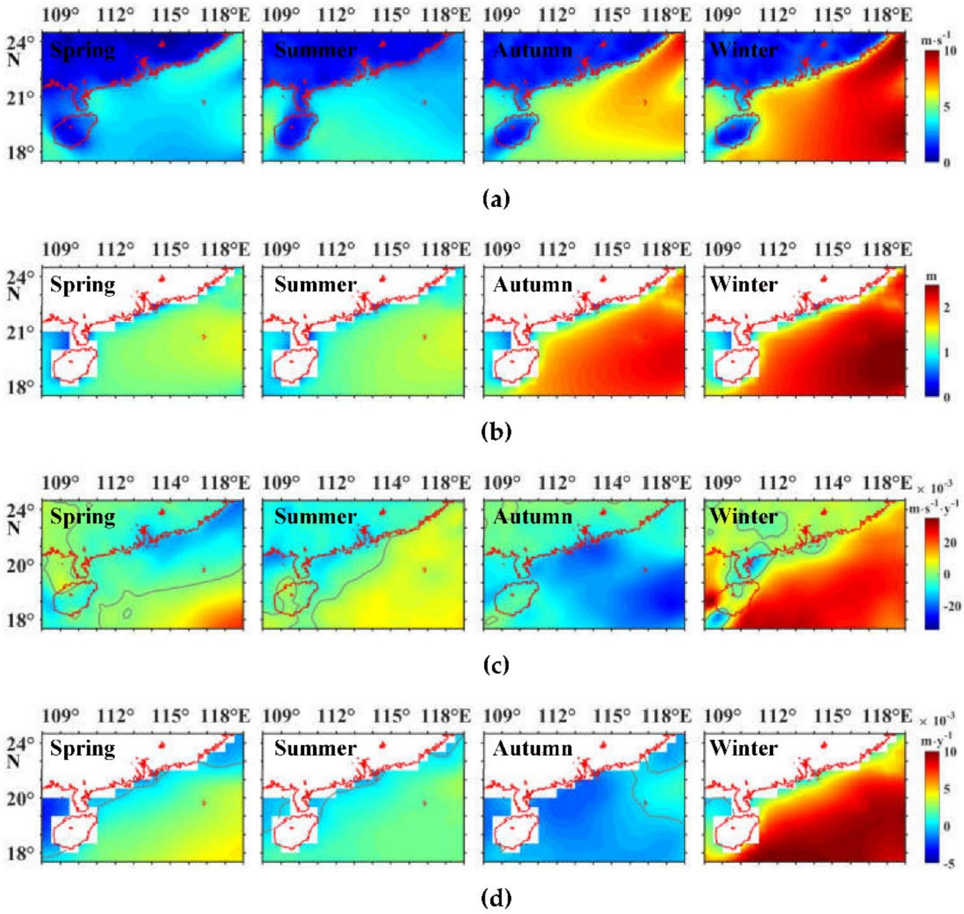

Figure 12. (**a**) Spatial distribution of the seasonal mean wind speed averaged from 1979 to 2019. (**b**) Spatial distribution of the seasonal mean significant wave height averaged from 1979 to 2019. (**c**) Trend of the seasonal mean wind speed. (**d**) Trend of the seasonal mean significant wave height. Grey represent are 0.

5. Conclusions

In this study, the latest ERA5 data were used to investigate the long-term trends of the wind field in the northern SCS over the past 41 years (1979–2019). The main conclusions are as follows.

The long-term trends of the wind field in the northern SCS showed significant spatial and seasonal variations. The wind speed in the coastal area has mainly decreased, whereas that in the open sea has mainly increased. The PRE and its adjacent sea, the coastal waters of the Leizhou Peninsula and the coastal waters of eastern Guangdong are three representative areas with significant decreasing trends in annual mean wind speed and strong wind days. The easterly wind component showed a significant weakening trend in the coastal and continental shelf area, whereas the northerly wind component showed an increasing trend in the open sea. The M–K mutation analysis of the wind field in the representative area indicated significant changes in the wind speed and frequency of strong winds in the coastal area of the northern SCS. The changes in the wind direction are minor.

The wind field in the northern SCS was significantly correlated with ENSO. The PCs of the dominant EOF modes and ONI were analyzed statistically using XWT and WTC. We found a significant negative correlation between the first mode PC and ENSO in the 3–6 year band. The second mode PC had a weaker correlation with ENSO, whereas both the phase and period were different at different timescales. A significant positive correlation was observed between the third mode PC and ENSO in the 4–6 year band.

The effect of climate change on the wind field has a significant effect on marine environmental factors. During 1979–2019, the upwelling along the east coast of Hainan Island and Guangdong showed an increasing trend. The strengthening of the wind stress curl was a major cause of the increase in coastal upwelling. The long-term trends of the significant wave height and wind showed similar spatial and seasonal variations. The long-term trends of the wind field play an important role in modulating the effect of climate change on wave height in the northern SCS.

Author Contributions: Conceptualization, B.H.; methodology, B.H. and J.Z.; validation, B.H. and J.Z.; formal analysis, J.Z. and B.H.; investigation, J.Z. and B.H.; resources, B.H.; data curation, J.Z.; writing—original draft preparation, J.Z. and B.H.; writing—review and editing, B.H.; visualization, J.Z.; supervision, B.H.; project administration, B.H.; funding acquisition, B.H. All authors have read and agreed to the published version of the manuscript.

Funding: This research was funded by the National Natural Science Foundation of China (Grant Nos. 41976014 and 51761135021) and the Key Research Program of Frontier Sciences, Chinese Academy Sciences (Grant No. QYZDJ-SSW-DQC022).

Institutional Review Board Statement: Not applicable.

Informed Consent Statement: Not applicable.

Data Availability Statement: Data available on request due to restrictions. The data presented in this study are available on request from the corresponding author. The data are not publicly available due to privacy.

Acknowledgments: We thank the editor and anonymous reviewers for their comments and suggestions. We thank the professional editing team from AsiaEdit for improving the manuscript.

Conflicts of Interest: The authors declare no conflict of interest.

References

1. Wang, B.; Huang, F.; Wu, Z.; Yang, J.; Fu, X.; Kikuchi, K. Multi-scale climate variability of the South China Sea monsoon: A review. *Dyn. Atmos. Oceans* **2009**, *47*, 15–37. [CrossRef]
2. Cui, K.; Sun, J.; Xue, F. Analysis of the spatial and temporal characteristics of sea surface wind field in the North Indian Ocean. Trans. *Oceanol. Limnol.* **2013**, *4*, 34–42. Available online: http://en.cnki.com.cn/Article_en/CJFDTOTAL-HYFB201304005.htm (accessed on 20 March 2021).
3. Parvathi, V.; Suresh, I.; Lengaigne, M.; Izumo, T.; Vialard, J. Robust Projected Weakening of Winter Monsoon Winds Over the Arabian Sea Under Climate Change. *Geophys. Res. Lett.* **2017**, *44*, 9833–9843. [CrossRef]
4. Dong, S.; Gong, Y.; Wang, Z. Long-term variations of wind and wave conditions in the Taiwan Strait. *Reg. Stud. Mar. Sci.* **2020**, *36*, 101256. [CrossRef]
5. Gai, C.; Liu, Q.; Roberts, A.P.; Chou, Y.; Zhao, X.; Jiang, Z.; Liu, J. East Asian monsoon evolution since the late Miocene from the South China Sea. *Earth Planet. Sci. Lett.* **2020**, *530*, 115960. [CrossRef]
6. Islek, F.; Yuksel, Y.; Sahin, C. Spatiotemporal long-term trends of extreme wind characteristics over the Black Sea. *Dyn. Atmos. Oceans* **2020**, *90*, 101132. [CrossRef]
7. Yang, C.; Dang, H.; Zhou, X.; Zhang, H.; Wang, X.; Wang, Y.; Qiao, P.; Jiang, X.; Jian, Z. Upper ocean hydrographic changes in response to the evolution of the East Asian monsoon in the northern South China Sea during the middle to late Miocene. *Glob. Planet. Chang.* **2021**, *201*, 103478. [CrossRef]

8. Tamburini, F.; Adatte, T.; Föllmi, K.; Bernasconi, S.; Steinmann, P. Investigating the history of East Asian monsoon and climate during the last glacial–interglacial period (0–140,000 years): Mineralogy and geochemistry of ODP Sites 1143 and 1144, South China Sea. *Mar. Geol.* **2003**, *201*, 147–168. [CrossRef]
9. Shi, N. Features of the East Asian winter monsoon intensity on multiple time scale in recent 40 years and their relation to climate. *J. Appl. Meteor. Sci.* **1996**, *7*, 175–182. Available online: http://en.cnki.com.cn/Article_en/CJFDTOTAL-YYQX602.006.htm (accessed on 20 March 2021).
10. Yang, M.; Xu, H.; Li, W.; Liu, Y. Variations of East Asian monsoon and its relationships with land-sea temperature in recent 40 years. *J. Appl. Meteor. Sci.* **2008**, *19*, 522–530. [CrossRef]
11. Jiang, Y.; Luo, Y.; Zhao, Z.; Tao, S. Changes in wind speed over China during 1956–2004. *Theor. Appl. Clim.* **2009**, *99*, 421–430. [CrossRef]
12. Jiang, Y.; Luo, Y.; Zhao, Z. Maximum wind speed changes over China. *Acta Meteorol. Sin.* **2013**, *27*, 63–74. [CrossRef]
13. Shi, P.-J.; Zhang, G.-F.; Kong, F.; Ye, Q. Wind speed change regionalization in China (1961–2012). *Adv. Clim. Chang. Res.* **2015**, *6*, 151–158. [CrossRef]
14. Mo, H.; Hong, H.; Fan, F. Estimating the extreme wind speed for regions in China using surface wind observations and reanalysis data. *J. Wind. Eng. Ind. Aerodyn.* **2015**, *143*, 19–33. [CrossRef]
15. Dai, N.; Xie, A.; Zhang, Y. Interannual and interdecadal variations of summer monsoon activities over South China Sea. *Clim. Environ. Res.* **2000**, *5*, 363–374. [CrossRef]
16. Zhang, X.; Li, J.; Ding, Y.; Yan, J. A study of circulation characteristics and index of South China Sea summer monsoon. *Acta Meteorol. Sin.* **2001**, *15*, 450–464. [CrossRef]
17. Liang, J.; Yang, S.; Li, C.; Li, X. Long-term changes in the South China Sea summer monsoon revealed by station observations of the Xisha Inland. *J. Geophys. Res-Atmos.* **2007**, *112*, D10104. [CrossRef]
18. Ward, M.N.; Hoskins, B.J. Near-surface wind over the Global Ocean 1949–1988. *J. Climate* **1996**, *9*, 1877–1895. [CrossRef]
19. Gulev, S.K.; Grigorieva, V. Last century changes in ocean wind wave height from global visual wave data. *Geophys. Res. Lett.* **2004**, *31*, 24302. [CrossRef]
20. Gulev, S.K.; Hasse, L. Changes of wind waves in the North Atlantic over the last 30 years. *Int. J. Climatol.* **1999**, *19*, 1091–1117. [CrossRef]
21. Gower, J.F.R. Temperature, Wind and Wave Climatologies, and Trends from Marine Meteorological Buoys in the Northeast Pacific. *J. Clim.* **2002**, *15*, 3709–3718. [CrossRef]
22. Young, I.R.; Zieger, S.; Babanin, A. Global Trends in Wind Speed and Wave Height. *Science* **2011**, *332*, 451–455. [CrossRef] [PubMed]
23. Wilson, R.E.; Swanson, R.L.; Crowley, H.A. Perspectives on long-term variations in hypoxic conditions in western Long Island Sound. *J. Geophys. Res. Space Phys.* **2008**, *113*, 12011. [CrossRef]
24. Scully, M. The importance of decadal-scale climate variability to wind-driven modulation of hypoxia in Chesapeake Bay. *Nat. Précéd.* **2009**, *40*, 1345–1400. [CrossRef]
25. Hong, B.; Wang, G.; Xu, H.; Wang, D. Study on the Transport of Terrestrial Dissolved Substances in the Pearl River Estuary Using Passive Tracers. *Water* **2020**, *12*, 1235. [CrossRef]
26. Yu, L.; Gan, J.; Dai, M.; Hui, C.R.; Lu, Z.; Li, D. Modeling the role of riverine organic matter in hypoxia formation within the coastal transition zone off the Pearl River Estuary. *Limnol. Oceanogr.* **2021**, *66*, 452–468. [CrossRef]
27. Zhao, H.; Dai, M.; Gan, J.; Zhao, X.; Lu, Z.; Liang, L.; Liu, Z.; Su, J.; Cao, Z. River-dominated pCO2 dynamics in the northern South China Sea during summer: A modeling study. *Prog. Oceanogr.* **2021**, *190*, 102457. [CrossRef]
28. Zhu, L.; Zhang, H.; Guo, L.; Huang, W.; Gong, W. Estimation of riverine sediment fate and transport timescales in a wide estuary with multiple sources. *J. Mar. Syst.* **2020**, *214*, 103488. [CrossRef]
29. Pan, J.; Gu, Y.; Wang, D. Observations and numerical modeling of the Pearl River plume in summer season. *J. Geophys. Res. Oceans* **2014**, *119*, 2480–2500. [CrossRef]
30. Jing, Z.; Qi, Y.; Du, Y. Upwelling in the continental shelf of northern South China Sea associated with 1997-1998 El Niňo. *J. Geophys. Res-Oceans.* **2011**, *116*, C02033. [CrossRef]
31. Lin, P.; Gan, J.; Hu, J. Coastal Upwelling in the Northern South China Sea. *Reg. Oceanogr. South China Sea* **2020**, *11*, 289–322. [CrossRef]
32. Shu, Y.; Wang, D.; Feng, M.; Geng, B.; Chen, J.; Yao, J.; Xie, Q.; Liu, Q.-Y. The Contribution of Local Wind and Ocean Circulation to the Interannual Variability in Coastal Upwelling Intensity in the Northern South China Sea. *J. Geophys. Res. Oceans* **2018**, *123*, 6766–6778. [CrossRef]
33. Wu, R.; Li, L. Summarization of study on upwelling system in the South China Sea. *J. Oceanogr. Taiwan Strait* **2003**, *22*, 269–276. [CrossRef]
34. Zhuang, W.; Wang, D.X.; Hu, J.Y.; Ni, W.S. Response of the cold water mass in the western South China Sea to the wind stress curl associated with summer monsoon. *Acta Meteorol. Sin.* **2006**, *25*, 1–13. [CrossRef]
35. Hersbach, H.; Bell, B.; Berrisford, P.; Hirahara, S.; Horanyi, A.; Muñoz-Sabater, J.; Nicolas, J.; Peubey, C.; Radu, R.; Schepers, D.; et al. The ERA5 global reanalysis. *Q. J. R. Meteorol. Soc.* **2020**, *146*, 1999–2049. [CrossRef]
36. Bonavita, M.; Hólm, E.; Isaksen, L.; Fisher, M. The evolution of the ECMWF hybrid data assimilation system. *Q. J. R. Meteorol. Soc.* **2016**, *142*, 287–303. [CrossRef]

37. Kendall, M.G. *Rank Correlation Methods*, 4th ed.; Charles Griffin: London, UK, 1975; p. 202.
38. Haktanir, T.; Bajabaa, S.; Masoud, M. Stochastic analyses of maximum daily rainfall series recorded at two stations across the Mediterranean Sea. *Arab. J. Geosci.* **2013**, *6*, 3943–3958. [CrossRef]
39. Gocic, M.; Trajkovic, S. Analysis of changes in meteorological variables using Mann-Kendall and Sen's slope estimator statistical tests in Serbia. *Glob. Planet. Chang.* **2013**, *100*, 172–182. [CrossRef]
40. Nyikadzino, B.; Chitakira, M.; Muchuru, S. Rainfall and runoff trend analysis in the Limpopo river basin using the Mann Kendall statistic. *Phys. Chem. Earth, Parts A/B/C* **2020**, *117*, 102870. [CrossRef]
41. Wei, F.Y. *Modern Statistical Diagnosis and Forecasting Techniques for Climate*, 2nd ed.; China Meteorological Press: Beijing, China, 2007.
42. Torrence, C.; Compo, G.P. A practical guide to wavelet analysis. *B. Am. Meteorol. Soc.* **1998**, *79*, 61–78. [CrossRef]
43. Yu, H.-L.; Lin, Y.-C. Analysis of space–time non-stationary patterns of rainfall–groundwater interactions by integrating empirical orthogonal function and cross wavelet transform methods. *J. Hydrol.* **2015**, *525*, 585–597. [CrossRef]
44. Grinsted, A.; Moore, J.P.; Jevrejeva, S. Application of cross wavelet coherence to geophysical time series. *Nonlinear Proc. Geoph.* **2004**, *11*, 561–566. [CrossRef]
45. Qi, Y.; Shi, P.; Mao, Q. Seasonal characteristics of the sea surface wind speed in the South China Sea by remote sensing. *Tropic. Oceanol.* **1996**, *15*, 68–73.
46. Qian, W.; Gan, J.; Liu, J.; He, B.; Lu, Z.; Guo, X.; Wang, D.; Guo, L.; Huang, T.; Dai, M. Current status of emerging hypoxia in a eutrophic estuary: The lower reach of the Pearl River Estuary, China. *Estuar. Coast. Shelf Sci.* **2018**, *205*, 58–67. [CrossRef]
47. Lorenz, E.N. *Empirical Orthogonal Functions and Statistical Weather Prediction*; Scientific Report No. 1; Massachusetts Institute of Technology: Cambridge, MA, USA, December 1956; p. 49.
48. Weare, B.C. El Niño and Tropical Pacific Ocean Surface Temperatures. *J. Phys. Oceanogr.* **1982**, *12*, 17–27. [CrossRef]
49. Wang, B.; Yang, J.; Zhou, T. Interdecadal Changes in the Major Modes of Asian–Australian Monsoon Variability: Strengthening Relationship with ENSO since the Late 1970s. *J. Clim.* **2008**, *21*, 1771–1789. [CrossRef]
50. Escribano, R.; Hidalgo, P. Spatial distribution of copepods in the north of the Humboldt Current region off Chile during coastal upwelling. *J. Mar. Biol. Assoc. U. K.* **2000**, *80*, 283–290. [CrossRef]
51. Messié, M.; Chavez, F.P. Nutrient supply, surface currents, and plankton dynamics predict zooplankton hotspots in coastal upwelling systems. *Geophys. Res. Lett.* **2017**, *44*, 8979–8986. [CrossRef]
52. Sverdrup, H.U.; Johnson, M.W.; Fleming, R.H. *The Oceans: Their Physics, Chemistry, and General Biology*; Prentice-Hall: Hoboken, NJ, USA, 1942.
53. Qiu, S.; Liang, C.; Dong, C.M.; Liu, Z. Analysis of the temporal and spatial variations in the wind and wave over the South China Sea. *J. Marin. Sci.* **2013**, *31*, 1–9. [CrossRef]
54. Zong, F.; Wu, K. Research on distributions and variations of wave energy in South China Sea based on recent 20 years' wave simulation results using SWAN wave model. *Transact. Oceanol. Limnol.* **2014**, *3*, 1–12.
55. Shimura, T.; Mori, N.; Hemer, M.A. Variability and future decreases in winter wave heights in the Western North Pacific. *Geophys. Res. Lett.* **2016**, *43*, 2716–2722. [CrossRef]
56. Aydoğan, B.; Ayat, B. Spatial variability of long-term trends of significant wave heights in the Black Sea. *Appl. Ocean Res.* **2018**, *79*, 20–35. [CrossRef]
57. Zheng, C.W.; Li, C.Y. Variation of the wave energy and significant wave height in the China Sea and adjacent waters. *Renew. Sustain. Energy Rev.* **2015**, *43*, 381–387. [CrossRef]